energies

MDPI

Article

Frequency–Stability–Domain-Based Coordinated Frequency Regulation Control Strategy for Wind Turbine and Electrolytic Aluminum Systems to Avoid Secondary Frequency Dip

Wei Chen [1,2], Fei Tang [3,*], Fangzheng Deng [3,*], Yixin Yu [3], Bincheng Li [3] and Xiayu Jiang [3]

1 Yunnan Power Grid Co., Ltd., Kunming 650011, China; chenwei_csg@163.com
2 Guangzhou Electric Power Trading Center Co., Ltd., Guangzhou 510663, China
3 School of Electrical Engineering and Automation, Wuhan University, Wuhan 430072, China; 2025282070264@whu.edu.cn (Y.Y.); 2025282070294@whu.edu.cn (B.L.); 2021302191560@whu.edu.cn (X.J.)
* Correspondence: tangfei@whu.edu.cn (F.T.); 2021302191549@whu.edu.cn (F.D.)

Abstract

In power systems with a high penetration level of wind power, wind turbines are required to temporarily extract stored rotor kinetic energy to provide primary frequency support, thereby compensating for the limited frequency regulation (FR) capability of the overall system. However, wind turbine participation may lead to underresponse (insufficient frequency support) or overresponse, potentially causing a secondary frequency dip (SFD). Electrolytic aluminum load (EAL), as an industrial load with FR potential, can rapidly adjust its active power input by controlling the electrolytic cell voltage, equivalently increasing the system's FR capacity and thereby enhancing the load disturbance resistance of power systems with high wind power penetration. This paper first analyzes the causes and mechanisms of the SFD induced by wind turbine overresponse based on a Unified transfer function structure (UTFS) model and introduces the concept of a frequency stability region. Within this region, the virtual droop and virtual inertia coefficients for wind turbines are tuned to prevent SFD during FR. Simultaneously, by involving EAL in system FR, the analysis reveals that its participation essentially equivalently expands the system's frequency stability region. Building on this analysis and considering spatiotemporal influencing factors, a coordinated wind-aluminum FR control strategy across multiple timescales is proposed to avoid SFD. Finally, a 39-bus simulation system built in DIgSILENT is used for validation. The simulation results indicate that the proposed control strategy effectively suppresses SFD under high wind power penetration conditions, and that the incorporation of EAL significantly expands the frequency stability region of the power system.

Keywords: electrolytic aluminum load; unified transfer function structure; primary frequency regulation; frequency stability region; integrated wind-aluminum frequency regulation

Check for updates

Academic Editor: Matilde Santos

Received: 10 March 2026
Revised: 7 April 2026
Accepted: 10 April 2026
Published: 15 April 2026

1. Introduction

1.1. Background and Literature Review

1.1.1. Background

In 2024, the National Development and Reform Commission, the National Energy Administration, and the National Data Administration jointly released the policy document entitled Action Plan for Accelerating the Construction of a New Type Power System

(2024–2027). The plan provides a strategic framework and an overall roadmap for advancing the development of a new-type power system in China. Its primary goal revolves around the twenty-character guideline of “clean and low-carbon, safe and sufficient, economical and efficient, supply-demand coordinated, flexible and intelligent,” aiming for breakthroughs in key areas to support the carbon peak target [1]. The utilization of new energy, as an essential pathway to achieve carbon peak, has become increasingly significant within China’s power system. However, the increasing penetration of renewable energy sources continuously displaces conventional generation, leading to a reduction in system inertia and a consequent degradation of primary frequency response capability [2,3]. This reduction diminishes its stability when facing frequency fluctuations. At present, renewable energy sources such as wind and photovoltaic generation are increasingly integrated into the power grid and contribute to FR. However, owing to the inherent intermittency and variability of their output, the capability of these resources to provide stable and sustained frequency support remains constrained. Furthermore, when the wind turbine rotor speed reaches its minimum threshold, the turbine initiates speed recovery, which can induce an SFD, significantly impacting the system’s frequency stability. Therefore, exploring novel FR resources on the load side to enhance power system stability represents a feasible approach requiring urgent investigation.

1.1.2. Research on Wind Power FR and the Potential of Load-Side Resources

The role of wind generation in system frequency control has attracted growing scholarly attention worldwide. In particular, the SFD phenomenon triggered during wind turbine frequency support has become a key issue of investigation in recent years. In [4,5], deloaded operation of doubly fed induction generators (DFIGs) is achieved through advanced control strategies, enabling the reservation of a certain level of active power margin. A droop controller is further embedded into the rotor-side active power control loop to facilitate participation in primary frequency response. Nevertheless, this approach does not sufficiently consider the intrinsic control dynamics of the DFIG. Moreover, the use of a constant droop coefficient limits adaptability, preventing full exploitation of the unit’s real-time available capacity, particularly under high wind speed conditions. Reference [6] investigated the coupling mechanism between the secondary frequency drop (SFD) phenomenon and wind turbine control strategies and subsequently derived appropriate frequency response coefficients to mitigate the occurrence of SFD at the system level. Reference [7] utilized demand response to identify the timing of SFD occurrence and provide compensation, thereby mitigating the depth of the dip. The impact of wind turbine frequency support control parameter settings on system-level frequency dynamic behavior was systematically investigated in [8]. By integrating indicators such as the initial frequency dip and the secondary dip, it tuned control parameters and explored parameter tuning rules under different wind power penetration levels. Reference [9] established a multi-objective optimization model for parameters including virtual inertia control, droop control for renewable energy, and load frequency control. Adjusting microgrid control parameters based on this model can reduce system frequency deviation and load shedding. Reference [10] proposed an analytical method to assess the impact of doubly-fed induction generator integration on system inertia level and frequency response process. To alleviate excessive frequency deviations during wind power participation, segmented frequency support combined with staged speed recovery has been explored, effectively reducing both the maximum frequency excursion and the severity of secondary dips [11]. In parallel, flexible frequency response strategies have been developed to address the inherent trade-off between mitigating SFD and achieving rotor speed restoration [12]. An additional power participation factor was formulated using piecewise and Logistic functions, through which

https://doi.org/10.3390/en19081912

the electromagnetic output power of wind turbines was regulated by adjusting corresponding shape coefficients. Nevertheless, the intrinsic FR capability of wind turbines remains inherently constrained. When the system's frequency stability margin is insufficient, tuning parameters alone cannot prevent excessive initial and SFD [6]. As generation-side FR resources are increasingly insufficient to satisfy the operational requirements of modern power systems, and large-scale energy storage solutions remain economically constrained under current technological conditions, it becomes imperative to explore alternative FR resources on the demand side to further enhance system stability. Among various load-side resources, EAL are characterized by concentrated energy consumption, thermal inertia, and favorable control characteristics. In Yunnan Province, China, they account for over 30% of the total load [13], presenting significant FR potential.

1.1.3. EAL for FR and System Frequency Response Analysis

A substantial body of international research has examined the involvement of EAL in power system FR. Reference [14] proposed a coordinated frequency control strategy integrating wind power generation and aluminum loads to support system frequency stability. This approach integrates a fast active power support scheme for wind turbines, developed on the basis of an improved virtual inertia control strategy, with load curtailment in the aluminum electrolysis process to provide coordinated support for grid FR. Reference [15], while investigating the use of frequency deviation as a feedback signal to regulate EAL power, also considered post-disturbance static voltage stability constraints. These constraints were used to determine the allocation of regulation amounts among multiple aluminum smelters participating in grid FR. Reference [16] introduced an energy recovery strategy associated with the participation of EALs in primary FR. This strategy enables the EAL to return to its original operating state as soon as possible after providing frequency support through load reduction. Moreover, with the increasing participation of renewable energy sources, controllable loads, and other devices in the FR of new-type power systems, the conventional system frequency response model [17] encounters significant limitations. In particular, the equivalent aggregation process often results in a high-order representation, which complicates the derivation of analytical time-domain solutions. Consequently, it is not well-suited for frequency response analysis in new type power systems. References [18,19] proposed a similar UTFS model. This model adopts a unified transfer function to characterize the active power–frequency response behavior of heterogeneous devices, thereby enabling a compact parameter representation while maintaining high accuracy in the analysis of frequency dynamics in new-type power systems.

1.2. Contribution and Organization

1.2.1. Contribution of This Paper

To address the SFD issue identified above, this paper proposes a coordinated primary frequency regulation strategy integrating EALs and wind power within the UTFS analytical framework. While the UTFS model draws on established methodologies, the key innovations of this work lie in the following aspects: first, based on the thermal inertia characteristics of the electrolytic cells and the production process of EAL, this paper proposes a reasonable power regulation strategy to ensure that the EAL can quickly respond to system frequency variations while maintaining production safety and stable output; second, the virtual inertia and virtual droop parameters that enable wind turbines to fully participate in frequency regulation are quantitatively derived; third, the frequency stability region is explicitly established; and finally, based on this stability region, a novel coordinated frequency regulation strategy for wind power and EALs is developed. The frequency regulation capability of EAL is evaluated, and its function in delivering power support

https://doi.org/10.3390/en19081912

during frequency response is equivalently represented as a generation-side unit. The UTFS model is then employed to investigate the underlying mechanism of the SFD phenomenon and to analyze the impact of wind turbine frequency regulation parameters on the occurrence and severity of SFD. By leveraging the derived optimal control parameters, the rotor kinetic energy is fully utilized while maintaining frequency security. Furthermore, using the frequency stability region as a criterion, a multi-timescale coordinated wind power and EAL frequency regulation control strategy is constructed. This method not only effectively resolves the SFD issue during the wind turbine speed recovery process but also enhances the power system's resilience against load disturbances.

1.2.2. Organization of This Paper

The organization of the manuscript is outlined in Figure 1. Section 2 examines the mechanism by which EAL participates in primary FR. Section 3 analyzes the UTFS model and determines the optimal parameters for wind turbine involvement in FR based on this framework. In Section 4, the concept of the frequency stability region is introduced, and a coordinated control strategy for EAL and wind turbines participating in system FR is developed accordingly. Section 5 presents case studies to validate the effectiveness and practical applicability of the proposed frequency stability region. Finally, conclusions are drawn in Section 6.

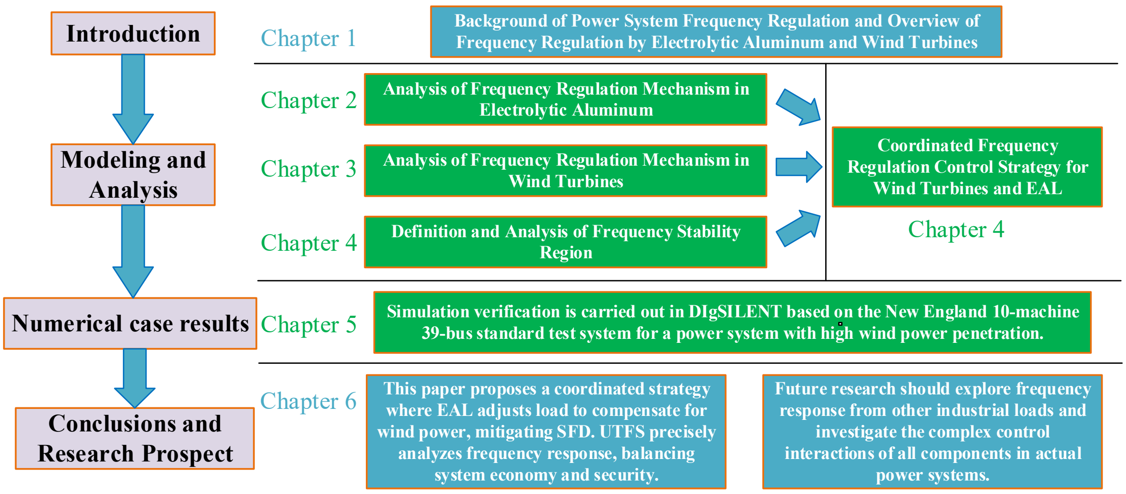

Figure 1. Structure of the article content.

2. EAL Model and Its FR Control

EAL is a typical high-energy-consumption industrial load [20]. Characterized by substantial power consumption, easily implementable response control, and minimal impact on normal production processes during short-term regulation, it represents an ideal demand-side response resource. This chapter first introduces the electrical model of the EAL, including its topological structure and process technology. This is followed by a focused analysis of the active power regulation method based on saturable reactors. Subsequently, the FR potential and control strategy of the EAL are examined.

2.1. EAL Modeling

The topological structure of the EAL is shown in Figure 2. Since electrolytic cells utilize low-voltage, high-current direct current during the electrolysis process [21], it is necessary to use a three-phase bridge rectifier system connected to the high-voltage AC busbar to collect electrical energy onto the DC busbar. The rectifier system comprises multiple parallel-connected rectifier circuits. The electrolytic cell, which converts aluminum oxide into aluminum metal, can be represented equivalently by a series connection of an equivalent resistance and a back electromotive force (back EMF).

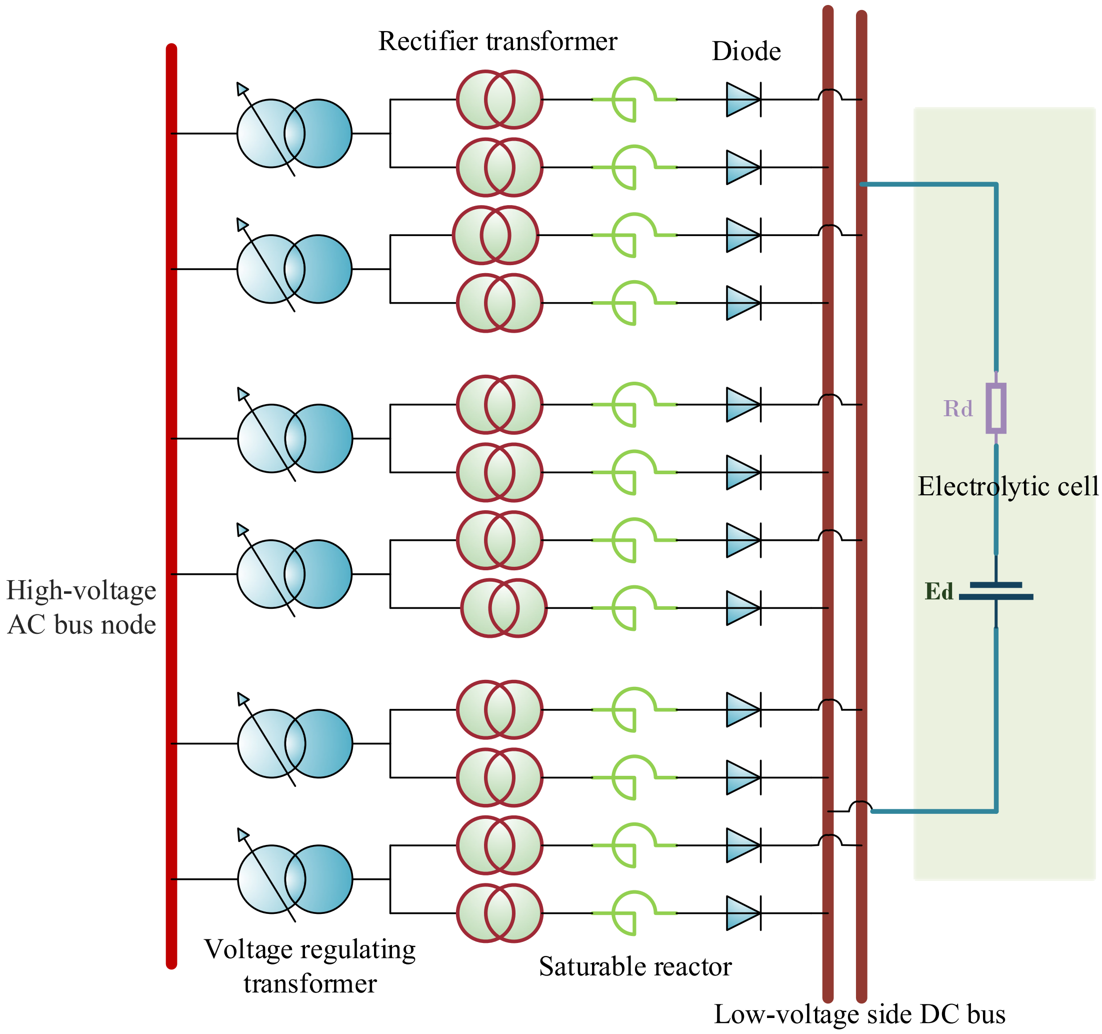

Figure 2. Topology of EAL.

For a specific aluminum smelter, the equivalent resistance R_d and the equivalent back EMF E_d can be considered constant, with values of 2.016 mΩ and 354.6 V, respectively [22]. Therefore, in conjunction with Figure 2, the active power P_d of the EAL can be expressed as shown in Equation (1):

$$\begin{aligned} P_d &= U_d I_d = \frac{U_d(U_d - E_d)}{R_d} \\ &= \frac{U_d(U_d - 354.6)}{2.016} \times 10^{-3} (\mathrm{MW}) \end{aligned} \quad (1)$$

where U_d is the DC voltage and I_d is the DC current. Therefore, the active power of the EAL is determined by the DC voltage U_d.

The equivalent circuit of the EAL is shown in Figure 3. There are three methods for regulating the active power of the EAL: adjusting the AC side voltage, adjusting the tap ratio of the on-load tap changer transformer, and adjusting the saturable reactor. Among these, the on-load tap changer offers relatively low regulation accuracy and is unsuitable for frequent operation, while the AC side voltage is difficult to regulate within a large power grid. In contrast, the saturable reactor enables fine voltage regulation at the millisecond level. Therefore, adjusting the saturable reactor is prioritized [23,24].

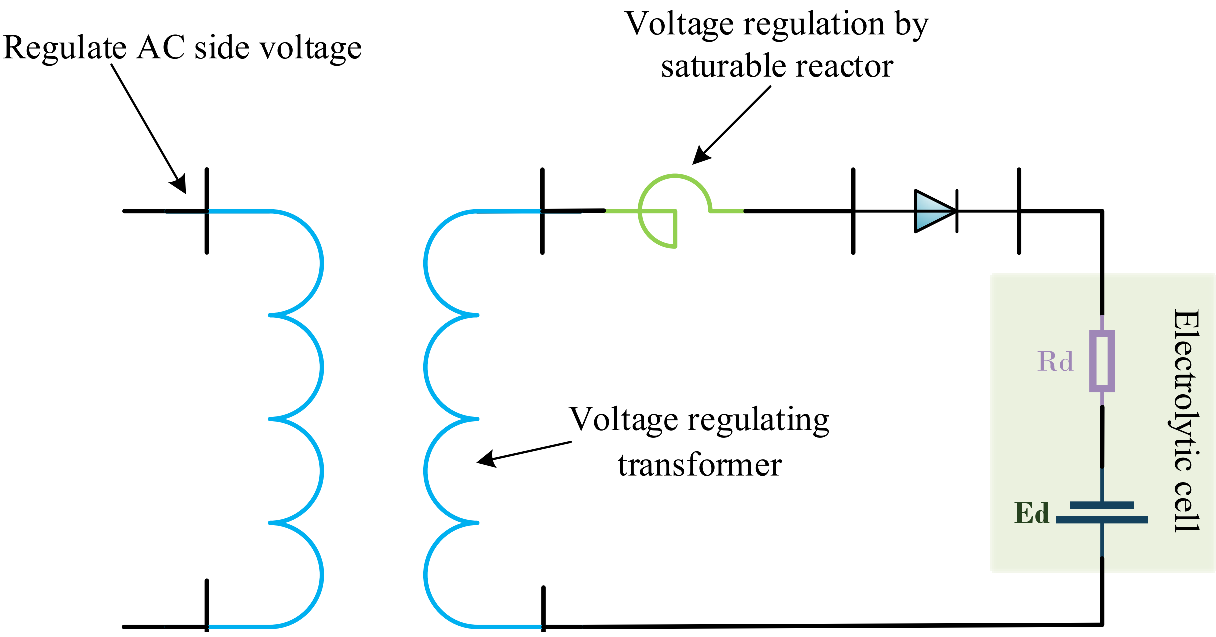

Figure 3. Active power regulation method for EAL.

The cosine of the commutation saturation angle α can be expressed by the control current I_c as shown in Equation (2):

$$\cos\alpha = \frac{\omega N_g A_t (B_b - \mu N_c I_c)}{\sqrt{6}E} \tag{2}$$

In Equation (2), w represents the grid angular frequency. The working winding consists of N_g turns, while A_t characterizes the effective cross-sectional area of the magnetic core. The magnetic properties are described by the saturation flux density B_b and the permeability μ. The control winding contains N_c turns and is driven by the control current I_c. The grid voltage magnitude is denoted by E, expressed in root-mean-square (RMS) form.

Based on these definitions, the rectifier's average output voltage U_d is obtained as shown in Equation (3):

$$\begin{aligned} U_d &= \frac{1}{\pi/3}\int_{-\frac{\pi}{3}+\alpha}^{\frac{\pi}{3}+\alpha} \sqrt{2}U_L \cos\omega t dt = \frac{3\sqrt{6}}{\pi}U_L \cos\alpha \\ &= \frac{3\sqrt{6}}{\pi}U_L + \frac{3\sqrt{3}}{\pi}\frac{\omega N_g A_t \mu N_c}{l} I_c = U_{d0} - k_{sr} I_c \end{aligned} \tag{3}$$

where U_L is the RMS line voltage, U_{d0} is the maximum DC voltage, and k_{sr} is the regulation coefficient of the saturable reactor.

2.2. Analysis of FR Potential of EAL

As an energy-intensive industrial load, EAL exhibits considerable potential for regulation. Its FR capacity primarily depends on its load reduction capability, which refers to the extent of active power reduction permissible while ensuring operational safety and avoiding substantial impacts on production requirements [22]. According to Equation (1), the active power of EAL can be regulated by adjusting the operating voltage and current of the electrolytic cell. However, considering practical constraints such as production requirements and equipment safety, the adjustment ranges of voltage and current are subject to certain limitations.

First, the stability of the electrolytic cell current is crucial for ensuring stable production of the EAL. A slight decrease in current may lead to reduced output without causing quality degradation or equipment damage. However, when the current drop exceeds 10%, it can directly cause production stagnation of the EAL process, resulting in significant impacts. Therefore, when the EAL participates in grid FR during production, the minimum current reduction is limited to 10%. Under this condition, the series voltage is as shown in Equation (4):

$$U_d' = (1 - 10\%) I_d R_d + E_d \tag{4}$$

The maximum available active power of the EAL is shown in Equation (5):

$$\Delta P_{\max 1} = P_d - (1 - 10\%) I_d U_d' \tag{5}$$

Furthermore, considering the voltage regulation capability limitation of the saturable reactor, the maximum available active power of the EAL is as shown in Equation (6):

$$\Delta P_{\max 2} = P_d - (U_d - U_{\max}^{SR}) I_d' \tag{6}$$

where $U_{\max}^{SR}$ is the maximum voltage regulation depth of the saturable reactor, which is determined by the parameters of the saturable reactor and generally ranges from 40 V to 70 V [23]. I_d' is the series current corresponding to the voltage regulation limit of the saturable reactor, given by Equation (7):

$$I_d' = \frac{(U_d - U_{\max}^{SR}) - E_d}{R_d} \tag{7}$$

Therefore, the maximum active power that can be provided by the EAL when participating in FR is as shown in Equation (8):

$$\Delta P_{\max} = \min\{\Delta P_{\max 1}, \Delta P_{\max 2}\} \tag{8}$$

2.3. Frequency Response of EAL

The active power output of EAL is fundamentally determined by the DC voltage of the electrolytic cell. Since grid frequency fluctuations do not directly influence this DC voltage, variations in system frequency alone cannot induce changes in EAL active power. To establish frequency-responsive behavior, the frequency deviation must be incorporated as a control feedback signal to adjust the saturable reactor. Through this mechanism, the active power of EAL can be dynamically modulated in accordance with system frequency variations.

When the system experiences a load disturbance, a FR dead zone is established to prevent the EAL from operating frequently due to minor disturbances. The load participates in the response only when the detected frequency exceeds the minimum action value f_{max}. Taking the system frequency deviation Δf as the input, the reference value I_{dref} of the electrolytic cell series current is adjusted through droop-inertia composite control. This modifies the active power of the EAL, providing power support to the system. To prevent excessive changes in the DC current of the electrolytic cell that could lead to production stagnation, a limiting link is also required to ensure the current drop does not exceed 10% [24]. The frequency response structure diagram for the EAL participating in FR is shown in Figure 4.

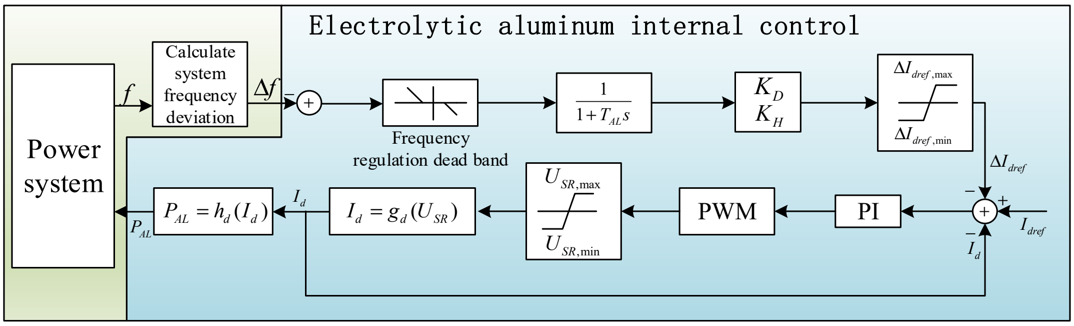

Figure 4. Frequency response block diagram of EAL.

3. UTFS of Power Systems and Tuning of Frequency Response Coefficients for Wind Turbines to Avoid SFD

Traditional analyses of SFD are constrained by the ASFR model and cannot adequately reflect the impact of different wind speeds and various operating states of wind turbines on frequency response. To address this issue, this section analyzes the influence of different wind turbine operating states on system frequency response based on the UTFS.

3.1. UTFS for Power Systems with High Penetration of Wind Power

This paper adopts a UTFS to simplify and replace detailed models of various power generation devices. This approach not only simplifies the analysis process but also ensures a certain degree of accuracy. The principle of the UTFS for power systems is to equivalently represent all power devices shown in Figure 5 by four parameters—H_{eq}, D_{eq}, K_{eq} and T_{eq}—when studying primary FR [25].

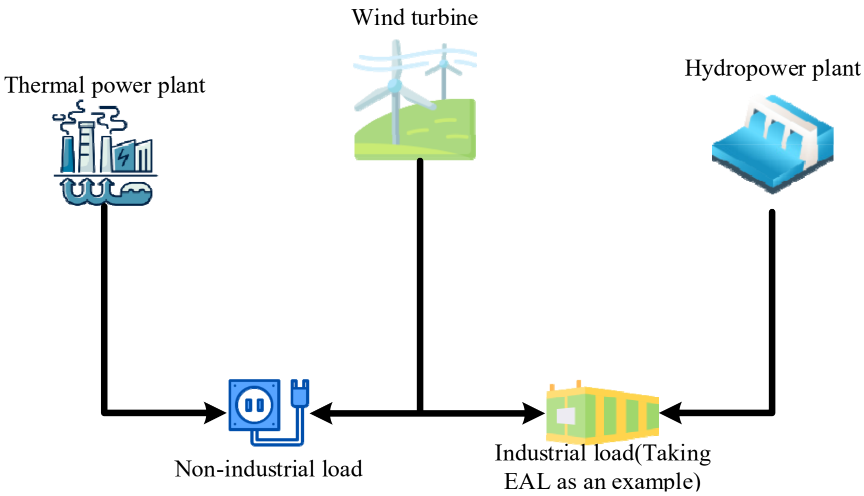

Figure 5. Components in a power system.

The frequency response expression under the UTFS is as shown in Equation (9):

$$\begin{cases} \Delta w_s = \Delta P_d \cdot \left(\frac{1}{2H_{eq}s + D_{eq} + \frac{K_{eq}}{1+T_{eq}s}} \right) \\ \Delta P_T = \Delta w_s \cdot \frac{K_{eq}}{1+T_{eq}s} \end{cases} \quad (9)$$

where Δw_s is the system frequency deviation, ΔP_d is the system disturbance power, and ΔP_T is the frequency response power. H_{eq}, D_{eq}, K_{eq}, and T_{eq} are all parameters of the UTFS. Referring to the ASFR parameters, H_{eq} is defined as the system equivalent inertia time constant, D_{eq} as the system equivalent load response coefficient, K_{eq} as the system equivalent droop coefficient, and T_{eq} as the system equivalent time constant of the droop response. Consequently, the system UTFS is illustrated in Figure 6.

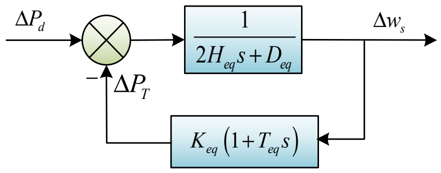

Figure 6. Unified transfer function structure (UTFS) model.

The focus of the UTFS is to ensure that the frequency change curve following a system disturbance fits the actual frequency change to the greatest extent possible. Therefore, solving for the model parameters is essentially a parameter optimization problem. As indicated by Reference [26], since the system frequency change is determined by all devices participating in frequency response, including synchronous units and renewable energy units involved in FR, this optimization problem can be decomposed into sub-optimization problems for the n generation devices in the system as shown in Equation (10):

$$\begin{cases} \min\limits_{H_i,D_i,K_i} & \int_{t_0}^{t_s} \left(\Delta P_{di}(t) - \Delta P'_{di}(t)\right)dt \\ s.t. & \Delta w(s) = \Delta P_{di}(s)\cdot G_i(s) \\ & \Delta w(s) = \Delta P'_{di}(s)\cdot G'_i(s) \\ & G_i(s) = \dfrac{1}{2H_i s + D_i + \dfrac{K_i}{1+T_{eq}s}} \end{cases} ,i = 1,2,\ldots,n \tag{10}$$

where $\Delta P_{di}(s)$ denotes the disturbance power effectively allocated to generation unit i, and $\Delta P_{di}{}'(s)$ represents the disturbance power equivalently distributed under the unified framework. These variables satisfy the power balance condition $\sum\Delta P_{di} = \Delta P_d$. Furthermore, $G_i(s)$ and $G_i{}'(s)$ correspond to the UTFS and its approximated form for generation unit i, respectively. Accordingly, the parameters of the unified structure in Equation (10) can be derived by applying linearization, leading to the formulation presented in Equation (11).

$$\begin{cases} \sum H_i = H_{eq} \\ \sum D_i = D_{eq} \\ \sum K_i = K_{eq} \end{cases} \tag{11}$$

Reference [18] employs a least-squares iterative algorithm to solve Equation (10). However, T_{eq} is also a quantity to be optimized. To improve solution accuracy, a dual-loop solution process (inner and outer loops) is adopted. Specifically, the outer loop first determines $T_{eq}(0)$, then enters the inner loop to optimize and solve for other parameters, obtaining the frequency response deviation under the equivalent unified structure parameters. The resulting frequency response deviation is evaluated and used to update the outer loop's $T_{eq}(0)$ value. This process is repeated, ultimately yielding the unified structure parameters under the optimal T_{eq}. The detailed solution process can be found in Reference [19].

Based on the system frequency-domain state equation, an analytical expression describing the system frequency in the frequency domain is obtained as shown in Equation (12):

$$\Delta f(s) = f_s \cdot \frac{w_n^2}{D_{eq} + K_{eq}} \cdot \frac{1 + T_{eq}s}{s^2 + 2\xi w_n s + w_n^2} \cdot \frac{\Delta P_d}{s} \tag{12}$$

In this formulation, f_s denotes the nominal system frequency, set to 50 Hz. The corresponding expressions for the system natural frequency and damping ratio are given by Equation (13):

$$\begin{cases} w_n^2 = \frac{D_{eq}+K_{eq}}{2H_{eq}T_{eq}} \\ \xi = \frac{2H_{eq}+\left(D_{eq}+K_{eq}\right)T_{eq}}{2\left(D_{eq}+K_{eq}\right)} \end{cases} \tag{13}$$

The maximum rate of change in frequency ($RoCoF_{max}$), which is the actual value expressed in Hz/s, is obtained by applying the Laplace initial value theorem (as shown in Equation (14)):

$$\left.\frac{df}{dt}\right|_{t=0} = f_s \cdot \frac{\Delta P_d}{2H_{eq}} \tag{14}$$

Therefore, the nadir of the initial frequency dip f_N is calculated through the inverse Laplace transform (as shown in Equation (15)).

$$f_N = f_s \cdot (1 + \frac{1}{K_{eq}+D_{eq}}\left[1 + \alpha e^{-\xi w_n t_{nadir1}} \sin\left(w_t t_{nadir1} + \phi\right)\right]\Delta P_d) \tag{15}$$

where

$$\begin{cases} \alpha = \sqrt{\frac{1-2T_{eq}\xi w_n + T_{eq}^2 w_n^2}{1-\xi^2}} \\ w_t = w_n\sqrt{1-\xi^2} \\ \phi = \tan^{-1}\left(\frac{w_t T_{eq}}{1-\xi w_n T_{eq}} + \tan^{-1}\left(\frac{\sqrt{1-\xi^2}}{\xi}\right)\right) \end{cases} \tag{16}$$

In Equation (16), all variables are defined as follows. The parameter α is an intermediate coefficient used in the analytical solution of the system frequency response. The symbol w_t denotes the damped natural angular frequency of the equivalent system. The variable w_n represents the undamped natural angular frequency, and ξ is the damping ratio of the system. The parameter T_{eq} denotes the equivalent time constant of the primary frequency response. The variable ϕ represents the phase angle associated with the system response.

Based on the above Equations (12)–(16), it can be observed that the system frequency indicators f_N and $RoCoF_{max}$ are related to the four parameters of the UTFS. Therefore, the essence of enhancing FR capability lies in modifying these four parameters of the UTFS to ensure that the aforementioned frequency indicators do not exceed their limits under larger load steps.

3.2. Tuning of Wind Turbine Frequency Response Coefficients to Avoid SFD

The mechanical power P_m captured by the wind turbine blades is given by Equation (17):

$$\begin{cases} P_{\mathrm{m}} = \frac{1}{2}\rho\pi R^2 v^3 C_{\mathrm{p}}(\lambda,\beta) \\ C_{\mathrm{P}} = 0.22\left(\frac{116}{\lambda_i} - 0.4\beta - 5\right)e^{-12.5/\lambda_i} \\ \frac{1}{\lambda_i} = \frac{1}{\lambda+0.08\beta} - \frac{0.035}{\beta^3+1} \\ \lambda = \frac{\omega_{\mathrm{r}} R}{v} \end{cases} \tag{17}$$

In this expression, ρ denotes the air density, while R represents the rotor radius of the wind turbine and v corresponds to the wind speed. The aerodynamic performance is characterized by the power coefficient C_P, which is determined by the blade pitch angle β and the tip speed ratio λ. The rotational speed of the wind turbine is indicated by w_r.

Under MPPT operation, the active power output of the wind turbine can be written as shown in Equation (18):

$$P_{MPPT}(v, w_r) = \begin{cases} \frac{1}{2}\rho\pi\frac{R^4}{\lambda^3}C_P w_r^3 \; w_r < w_{r\max} \\ P_{\max} \;\; w_r > w_{r\max} \end{cases} \tag{18}$$

where λ is the optimal tip speed ratio, and $w_{r\max}$ is the maximum allowable wind turbine rotational speed.

When wind turbines participate in system FR through virtual inertia and virtual droop control, the following applies (as shown in Equation (19)):

$$\begin{cases} P_{ref}(v, w_r) = P_{MPPT}(v, w_r) + \Delta P \\ \Delta P = -k_H\frac{df}{dt} - k_D\Delta f \end{cases} \tag{19}$$

where k_H is the virtual inertia coefficient, and k_D is the virtual droop coefficient. Their values determine the magnitude of H, D, K when the wind turbine participates in the system frequency response.

The fundamental mechanism underlying wind turbine participation in FR lies in temporarily reducing the rotor speed, thereby releasing part of the stored rotational kinetic energy to provide additional active power and compensate for system power deficits. When the rotor speed decreases to its lower operational limit, a speed recovery process is triggered. At the onset of this recovery stage, the active power output of the wind turbine exhibits an instantaneous reduction. In this study, only the constant-power speed recovery mode is considered, in which the reference value of active power during the recovery phase remains unchanged. The corresponding variations in wind turbine active power output and system frequency are illustrated in Figures 7 and 8.

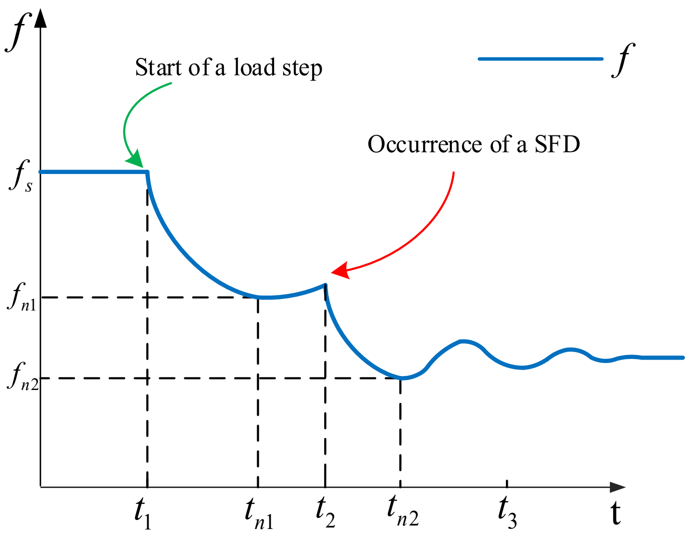

Figure 7. System frequency trajectory when the SFD occurs.

To ensure that the wind turbine does not experience an SFD during the FR process, it is necessary to ensure that the FR parameters k_H and k_D of the wind turbine are not set too high. However, if these parameters are set too low, the FR capability of the wind turbine cannot be fully utilized. Therefore, it is essential to calculate the optimal parameters for the wind turbine. This paper assumes a short-term wind speed forecast resolution of 5 min, disregarding forecast accuracy issues, while the system periodically checks the operating status of each generation unit at this resolution.

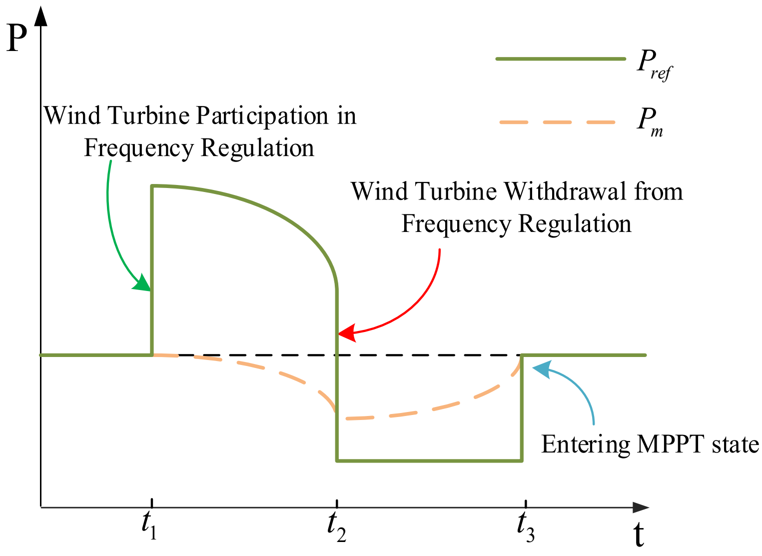

Figure 8. Wind power trajectory when the SFD occurs.

At t_{n1}, the wind turbine needs to fully utilize the rotor kinetic energy. According to Equations (17)–(19), the result is obtained as shown in Equation (20):

$$\int_{t_1}^{t_{n1}} P_{ref}(v,w_r) - P_m(v,w_r)dt = \frac{1}{2}J\left(w_{iwts}^2 - w_{\min}^2\right) = \Delta E_k \quad (20)$$

where J is the rotational inertia of the wind turbine rotor.

Based on the above, the calculation results are as shown in Equation (21):

$$\begin{aligned}\int_{t_1}^{t_{n1}} P_{ref}(v,w_r)dt &\approx \int_{t_1}^{t_{n1}} \frac{1}{2}\Big(P_{ref}(v,w_{iwts}) + P_{ref}(v,w_{\min})\Big)dt \\ &= \frac{1}{2}\Big(P_{ref}(v,w_{iwts}) + P_m(v,w_{\min})\Big)t_{n1}\end{aligned} \quad (21)$$

Assume the fault disturbance time t_1 = 0. The mechanical power $P_m(v,w_r)$ satisfies the differential incremental calculation (as shown in Equation (22)):

$$\int_0^{t_{n1}} P_m(v,w_r)dt = \int_0^{t_{n1}} P_m(v,w_{iwts}) + \Delta P_m(v,w_r)dt \quad (22)$$

Assuming the wind speed remains constant during the frequency response process, and using Taylor expansion for differential calculation (as shown in Equation (23)):

$$\begin{aligned}&\Delta P_m(v,w_r) = \frac{1}{2}\rho\pi R^2 v^3 \cdot \Delta C_p(\lambda,\beta) \\ &= \frac{1}{2}\rho\pi R^2 v^3 \sum_{k=1}^{n} \frac{1}{k!}\frac{\mathrm{d}^k C_p}{\mathrm{d}t^k}\bigg|_{t=0}(t-t_1)k\end{aligned} \quad (23)$$

Assuming that w_r changes at a constant rate during the frequency response process, its second-order Taylor differential can be calculated as shown in Equation (24):

$$\begin{cases} \frac{\partial C_p}{\partial t}\big|_{t=0} = \frac{\partial C_p}{\partial \lambda}\frac{\partial \lambda}{\partial w_r}\frac{\partial w_r}{\partial t}\big|_{t=0} = \frac{R}{v}\frac{\partial C_p}{\partial \lambda}\frac{\partial w_r}{\partial t}\big|_{t=0} \\ \frac{\partial^2 C_p}{\partial t^2}\big|_{t=0} = \left(\frac{R}{v}\right)^2 \frac{\partial^2 C_p}{\partial \lambda^2}\left(\frac{\partial w_r}{\partial t}\right)^2\big|_{t=0} + \frac{R}{v}\frac{\partial C_p}{\partial \lambda}\frac{\partial^2 w_r}{\partial t^2}\big|_{t=0} \end{cases} \quad (24)$$

Combining Equations (22)–(24), the variation in the mechanical energy of the wind turbine during the frequency response can be obtained as shown in Equation (25):

$$\begin{aligned}\int_0^{t_{n1}} P_m(v,w_r)dt \quad &= P_m(v,w_{iwts})\cdot t_{n1}+\\ &\frac{1}{2}\rho\pi(R^3v^2\frac{\partial C_p}{\partial\lambda}|_{t=0}\cdot\Delta w_r+\\ &\frac{1}{3}R^4v^2\frac{\partial^2 C_p}{\partial\lambda^2}|_{t=0}\cdot\Delta w_r^2)\cdot t_{n1}\end{aligned} \tag{25}$$

According to Equations (20), (21) and (25), the maximum power command value $P_{ref}(v,w_{iwts})$ of the wind turbine at the initial moment t_1 of the frequency response can be derived as shown in Equation (26):

$$P_{ref}(v,w_{iwts}) = \frac{2}{t_{n1}}\left(\Delta E_k + \int_0^{t_{n1}} P_m(v,w_r)dt\right) - P_m(v,w_{\min}) \tag{26}$$

The wind speed affects the tuning of frequency response parameters. Assuming consistent wind speed within the same wind farm, the frequency response control parameters for wind turbines within the wind farm nn to avoid an SFD can be calculated as shown in Equation (27).

$$\begin{cases} k_{Hi} = \frac{P_{ref\max n} - P_{MPPT}(v_n,w_{iwts})}{RoCoF_{\max}} & t=0 \\ k_{Di} = \frac{P_m(v_n,w_{\min}) - P_{MPPT}(v_n,w_{\min})}{\Delta f_N} & t = t_{n1} \end{cases} \tag{27}$$

where $P_{refmaxn}$ and $P_m(v_n,w_{min})$ represent the maximum adjustable power $P_{ref}(v,w_{iwts})$ of the wind turbine in the wind farm and the captured mechanical power, respectively. Here, $\Delta P_d(t_1)$ and t_{N1} correspond to the maximum power disturbance ΔP_{dmax} occurring at the boundary of the system frequency nadir stability region and the moment of the nadir t_{N1}. $RoCoF_{max}$ and Δf_N correspond to the maximum rate of change in frequency and the maximum frequency deviation at the nadir on the system frequency stability boundary, respectively.

4. Control Strategy for EAL-Assisting Wind Turbine Frequency Response

The parameter settings for the wind turbine frequency response in Section 3.2 can avoid the occurrence of SFD under small power disturbances ($\Delta P_d(t_1) < \Delta P_{dmax}$). However, when the power disturbance is too large, the forced initiation of the wind turbine speed recovery strategy still occurs, potentially causing the maximum rate of change in frequency ($f_{RoCoFmax}$) and the frequency nadir (f_N) to exceed thresholds. Therefore, this section calculates the system "frequency stability region" using the UTFS and introduces EAL to enhance the system frequency stability margin.

4.1. EAL Response Expanding the System Frequency Stability Region

Within the UTFS framework, the system frequency stability region is defined as the set of disturbance power levels that satisfy the frequency safety constraints under the current UTFS parameters. The boundary of this region corresponds to the maximum step load disturbance that the system can withstand without triggering protective relays.

From Equations (6), (7) and (9), it is evident that the two primary system frequency indicators are linearly related to ΔP_d. Once the system unified structure parameter matrix $S_0(H_{eq},D_{eq},K_{eq},T_{eq})$ is determined, the linear relationship between these two primary frequency indicators and ΔP_d is established. Reformulating Equations (13)–(16) yields the following two expressions (as shown in Equations (28) and (29)):

$$\Delta P_{d\max 1} = \frac{2RoCoF_{\max}H_{eq}}{f_s} \tag{28}$$

$$\Delta P_{d\max2} = \frac{(f_N - f_s)(K_{eq} + D_{eq})}{f_s \cdot \left[1 + \alpha e^{-\xi w_n t_{nadir1}} \sin\left(w_t t_{nadir1} + \phi\right)\right]} \tag{29}$$

The system frequency stability margin must satisfy both primary frequency indicators; therefore, as shown in Equation (30):

$$\Delta P_{d\max} = \min\{\Delta P_{d\max1}, \Delta P_{d\max2}\} \tag{30}$$

When $\Delta P_d < \Delta P_{dmax}$, the system frequency is stable; otherwise, the system frequency becomes unstable.

When $\Delta P_d > \Delta P_{dmax}$ and the system frequency lies within the unstable region, introducing EAL for FR improves the system frequency stability.

After the EAL participates in FR, the FR capacity of the system increases, and the parameters of the UTFS change. At this time: $H_{eq} = H_{al} + H$, $D_{eq} = D_{al} + D$ and $K_{eq} = K_{al} + K$. Substituting these into the equations, the new frequency stability margin $\Delta P_{dmax}{}'$ of the system can be determined. Therefore, introducing EAL for FR is equivalent to increasing the frequency stability margin of the system.

4.2. Coordinated Wind Power and EAL Frequency Response Control Strategy

In Section 3.2, the tuning of wind turbine frequency response parameters depends on the wind speed v and the frequency stability margin boundary values $RoCoF_{max}$ and Δf_N. As described in Section 4.1, $RoCoF_{max}$ and Δf_N are determined by the dominant frequency stability issues of the system, which are related to the operating state of conventional units, specifically the parameter matrix $S_0(H_{eq},D_{eq},K_{eq},T_{eq})$. Meanwhile, the maximum power disturbance at the system stability boundary ΔP_{dmax} is determined by the unified structure parameter matrix $S_1(H_{eq},D_{eq},K_{eq},T_{eq})$ when wind turbines participate in frequency response. The massive number of power generation devices in the system and the complex and variable wind speeds make these calculations computationally intensive, failing to meet the time requirements for primary FR. Therefore, the FR strategy proposed in this paper comprehensively accounts for the spatial and temporal factors affecting system frequency response and presents a coordinated frequency control scheme integrating wind power and EAL to mitigate SFD. The offline calculation is performed at a time scale of five minutes, during which the operating status of each power device is updated and the wind speed for the following five minutes is forecasted. System parameters can be tuned offline, and the maximum frequency margin ΔP_{dmax}, along with the corresponding $RoCoF_{max}$ under this margin, can be calculated. These values are updated every five minutes to ensure the validity of the system's FR parameters while accommodating minor delays in the communication link and measurement process. Real-time detection involves continuous monitoring of the system frequency f. The UTFS assumes that the system frequency remains consistent across all grid locations—an assumption verified by simulation results showing near-identical frequency at all nodes. Consequently, FR devices only need to monitor the local grid frequency in real time. According to Reference [27], the associated delay can be reduced to 20–40 ms, satisfying the time-scale requirements of primary FR. The proposed coordinated wind-aluminum FR control strategy is illustrated in Figure 9.

The system control center tunes the frequency response parameter sequences k_{Hi} and k_{Di} using Equation (27) based on the 5 min wind speed forecast sequence for each wind farm, thereby calculating the unified structure model participation and the frequency stability region when wind turbines participate in FR with these parameters. To avoid excessively frequent participation of wind turbines in frequency response, a FR deadband is introduced. When the system frequency deviation remains within this deadband, the wind turbines will not participate in system FR. As shown in Figure 9, the condition for EAL to participate in system FR is that the real-time $RoCoF_{maxT}$ exceeds the $RoCoF_{max}$ value the system can withstand. This $RoCoF_{max}$ threshold can be obtained offline using Equation (14), thereby preventing EAL from being activated too easily. Reference [16] points out that the large thermal inertia of the electrolytic cells implies that a single primary FR event does not cause significant harm, but the cumulative effect of multiple events can be substantial. Therefore, the hierarchical FR strategy proposed for wind turbines and EAL not only enhances the system frequency stability margin but also takes the safety and stability of the EAL plant into consideration to a certain extent.

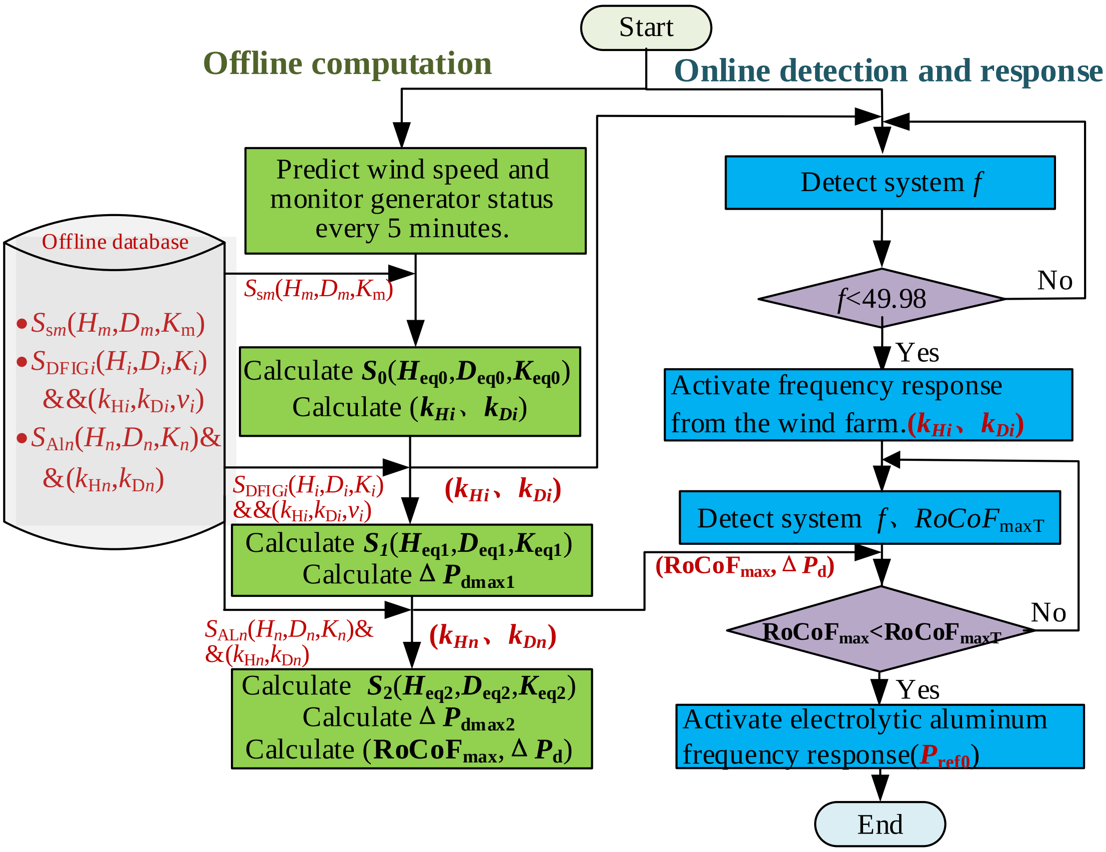

Figure 9. Integrated wind farm and EAL FR control strategy.

The decision for the EAL plant to participate in FR is based on comparing $RoCoF_{max}$ with $RoCoF_{maxT}$. This system comprises two parts: offline calculation and online detection. The online detection part monitors the system's rate of change in frequency and the frequency nadir, while the offline calculation part determines the system's UTFS parameters and the corresponding $RoCoF_{max}$.

It is worth noting that the proposed control strategy does not alter the existing under-frequency load shedding (UFLS) settings; instead, it serves as a fast front-end support measure, forming hierarchical coordination with UFLS. A coordinated relationship is established between electrolytic aluminum load FR and conventional under-frequency load shedding, characterized by "fast response in the first line, backup shedding in the second line".

5. Numerical Case Results

To verify the effectiveness of the UTFS model in the primary FR process of power systems with high wind power penetration, a power system with high wind power penetration was constructed on the DigSILENT platform based on the New England 10-machine 39-bus standard test system, as shown in Figure 10. Subsequent simulation verifications are all based on this system. Set the maximum allowable rate of change in frequency for the system as: $|RoCoFmax|$ = 0.5 Hz/s, and the frequency nadir as: f_N = 49.3 Hz.

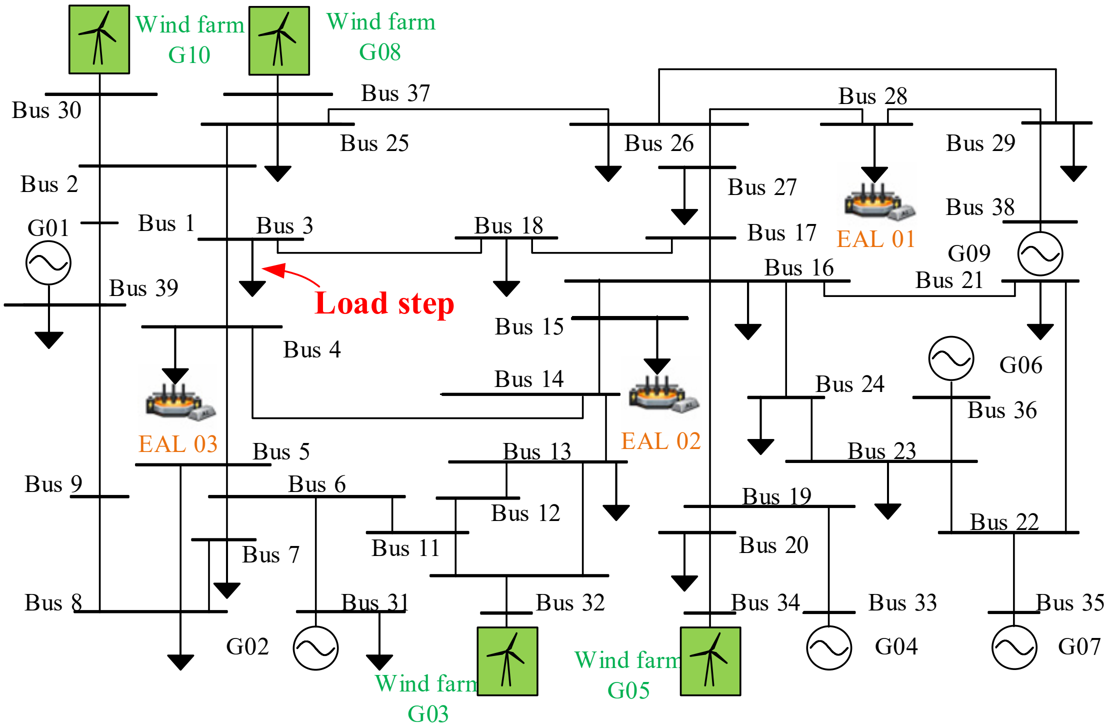

Figure 10. Power system model incorporating wind power and EAL.

As illustrated in Figure 10, the G03, G05, G08, and G10 wind farms are modeled as equivalent DFIG-based wind plants with different installed capacities. Within each individual wind farm, wind speed conditions are assumed. Aside from the frequency response module settings, all remaining control parameters are maintained consistently across the four wind farms, with detailed operating parameters provided in Table 1. As shown in Table 1, wind farms G05 and G10 in the simulation are set at the extreme conditions of cut-out and cut-in wind speeds, respectively, which helps verify that our coordinated control strategy remains effective under cut-in and cut-out wind speed conditions.

Table 1. Operating parameters of each DFIG wind farm.

	G03	**G05**	**G08**	**G10**
Number of units	1625	264	900	1075
P_e (MW)	660	301	540	246
v (m/s)	7	10	8	5.8
w_r (pu)	0.82	1.20	0.98	0.71
k_H	0.2	0.4	0.3	0
k_D	0.2	0.4	0.3	0

The total grid-connected capacity of the four DFIG wind farms reaches 1714 MW, corresponding to a wind power penetration level of 28%. According to Equation (18), the operational speed limits of the DFIGs are constrained between 0.7 pu and 1.2 pu. To avoid turbine tripping caused by excessive rotor speed reduction during frequency support, the virtual inertia and virtual droop gains of the G10 wind farm are deactivated. For the remaining wind farms, the frequency response coefficients are configured in proportion to the rotor speed w_{rmax}.

The grid-side converter capacity is limited to 1.2 pu. When the reference power P_{ref} exceeds this threshold, the actual grid-connected output of the wind turbine is capped at 1.2 pu.

At buses 4, 15, and 28, EAL with rated powers of 1000 MW, 800 MW, and 1200 MW, respectively, are used to replace the original loads. Initially, the EAL does not participate in system FR. According to Reference [28], the power reduction of EAL during frequency regulation should preferably not exceed 10% of its rated power. Therefore, the total active power regulation of all EALs in this simulation system is at most 300 MW.

The topology of the simulation system is identical to that of the standard test case. The total active power load level of the system is 6097 MW. The system rated frequency is modified to 50 Hz, and the power base value is 100 MVA.

G01, G02, G04, and G09 are conventional reheat gas turbine generating units, employing the IEEEG1 governor model as shown in Figure 10, with different operating parameters set, as detailed in Table 2. G06 and G07 are hydroelectric units, utilizing the IEEEG3 governor model. The parameters for each device are presented in Table 3. Among these, the IEEEG1 and IEEEG3 control parameters not mentioned in Tables 2 and 3 are set to 0. The grid-connected power of the synchronous generation units is 4389 MW, accounting for 72% of the total output level.

Table 2. Parameters of IEEEG1 governor for reheat steam turbine units.

	P (MW)	H_s(s)/K	T_1/T_3	T_4/T_5	T_6/T_7	K_1/K_3	K_5/K_7
G01	1120	5/20	0.2/0.2	0.4/0.05	12/0.4	0.2/0.2	0.35/0.25
G02	595	3.03/20	0.1/0.2	0.3/0.05	9/0.4	0.3/0.32	0.18/0.2
G04	632	2.86/18.2	0.1/0.1	0.2/0.05	9/0.4	0.3/0.26	0.3/0.16
G09	830	3.45/20	0.3/0.25	0.4/0.05	9/0.5	0.2/0.26	0.35/0.2

Table 3. Parameters of IEEEG3 governor for hydroelectric units.

	P (MW)	H_s(s)/R_P	R_T/T_G	T_P/T_R	T_W	a_{11}/a_{13}	a_{21}/a_{23}
G06	650	4.1/0.04	0.3/0.2	0.04/5	1	0.5/1	1.5/1
G07	562	4.2/0.04	0.2/0.05	0.04/10	0.75	0.5/1	1.5/1

A power disturbance of 6.44 p.u. is suddenly applied at Bus 3 at 10 s. The active power-frequency response characteristics of each generation device and the system common-mode frequency are analyzed. The UTFS parameters for thermal and hydro units are solved on a per-unit basis, while those for DFIG wind farms are solved on a per-wind-farm basis. After determining the UTFS parameters for each generation device in the system, the UTFS parameters for the overall system are solved.

Following the additional disturbance, the frequency variations at all system nodes can be obtained. Based on the system active power-frequency response relationship shown in Figure 6, the particle swarm optimization algorithm is employed to obtain the initialized system UTFS parameters and the initialized common-mode frequency, with the objective of minimizing the frequency deviation. The obtained UTFS parameters for the system are $S_0(H_{eq},D_{eq},K_{eq},T_{eq})$ = S_0(10.13,8.32,16.94,9.98). As indicated in Reference [29], the UTFS model requires comparison with time-domain simulation results. To further verify the effectiveness and accuracy of the system UTFS parameters S_0 in fitting the system frequency response under different power disturbances, various fault disturbances are set for simulation verification, as specifically shown in Figure 11.

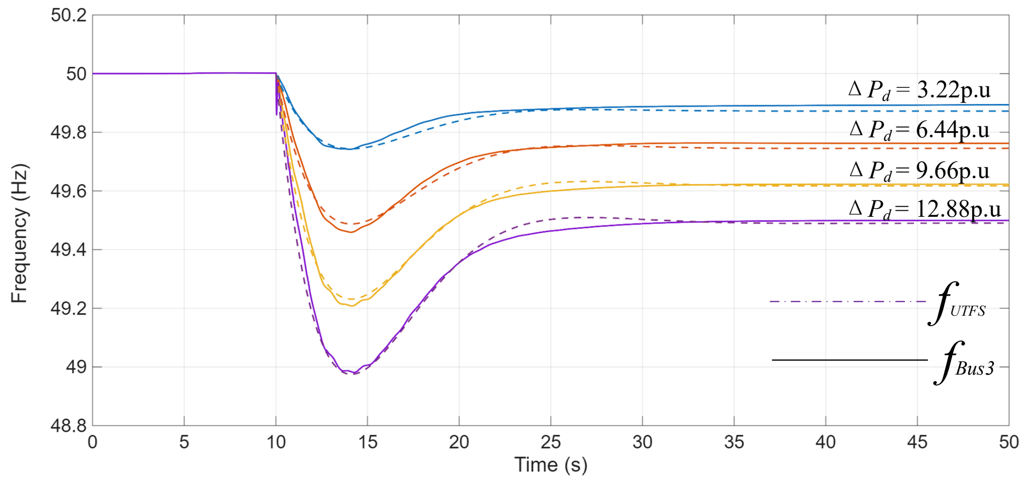

Figure 11. Comparison chart of system frequency response between real-time simulation and UTFS under different load steps.

To ensure that multiple independent PSO initializations converge to the same parameter neighborhood, the convergence trajectory plots of the fitness function across multiple runs are presented in Figure 12, where different colors represent the respective run orders and the thick black curve represents the average.

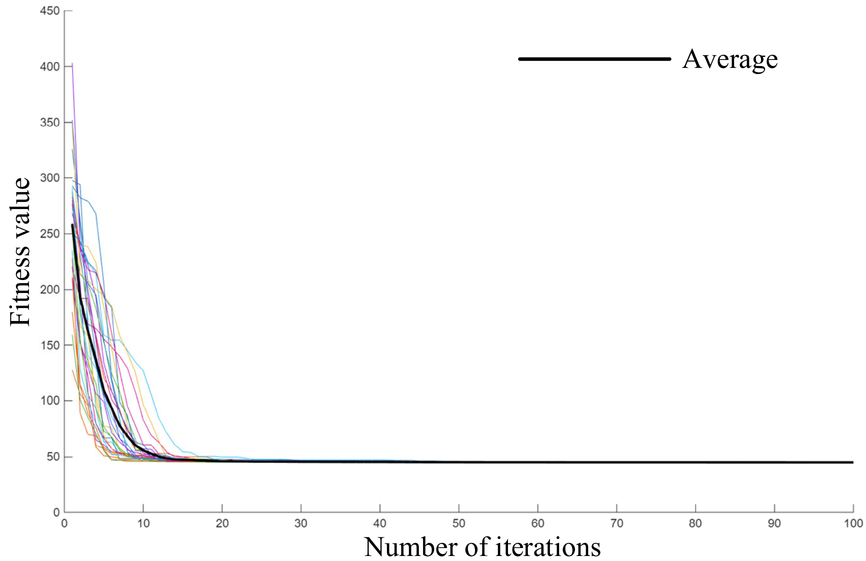

Figure 12. Fitness evolution curves for 30 runs.

According to Equation (27), the virtual inertia coefficient k_{H} and virtual droop coefficient k_{D} for different wind farms can be tuned, as shown in Table 4.

Table 4. Frequency response coefficients of each wind farm.

	G03	G05	G08
k_{H}	1.94	7.60	5.15
k_{D}	0.206	0.650	0.333

When all wind farms respond with the tuned parameters, the equivalent UTFS parameters of the system are S_1(45.56,12.92,4.71,9.93). As shown in Table 4, the virtual inertia coefficients k_{H} of different wind farms are larger than their virtual droop coefficients k_{D}. This is because the virtual inertia response power plays a major role in the initial stage of primary FR, while the virtual droop response power is present throughout the entire primary FR phase. The higher k_H enhances the system's ability to "resist" frequency decline. Compared to S_0, the system's equivalent inertia time constant *Heq* is now higher, and the time scale of the primary FR becomes slower.

The frequency response processes of the system under different power disturbances are specifically shown in Figure 13. According to the simulation results, when ΔP_d = 11.27 p.u., f_N = 49.3 Hz, and ∣*RoCoF*$_{max}$∣ is much lower than 0.5 Hz/s. At this point, the maximum power disturbance ΔP_{dmax1} = 11.27 p.u that the system can withstand is approximately 11.27 p.u. That is, when only wind turbines participate in system FR, the frequency stability margin boundary is ΔP_d = 11.27 p.u. When ΔP_d = 11.27 p.u., the active power output and rotational speed variation curves of the wind farms are shown in Figures 14 and 15.

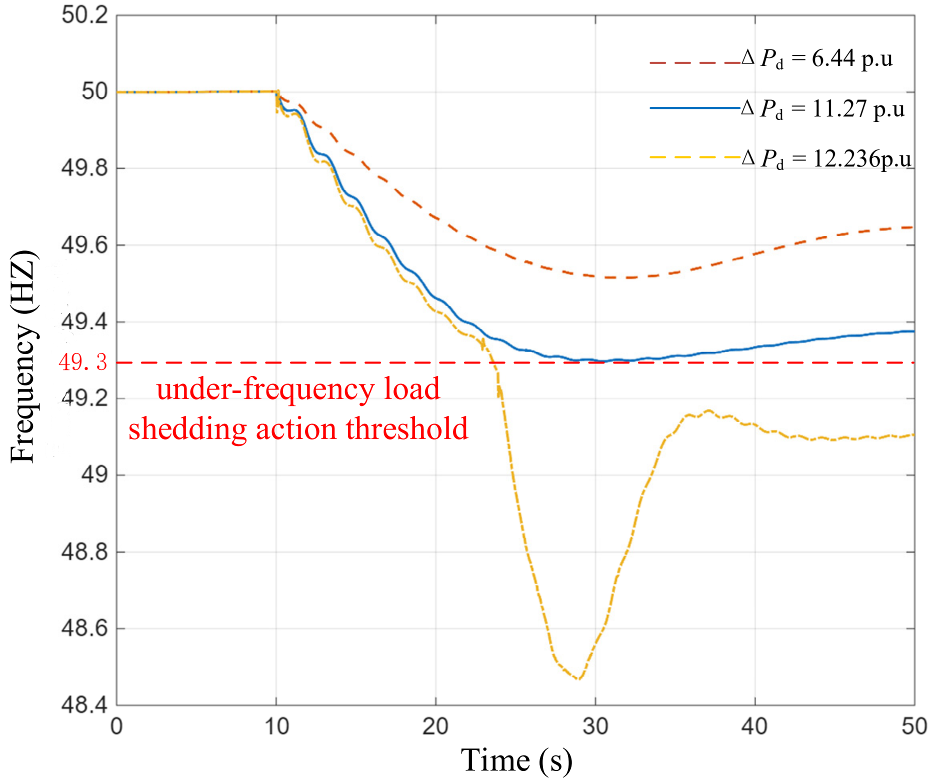

Figure 13. Frequency response curves of the system under different load steps when wind turbines participate in FR.

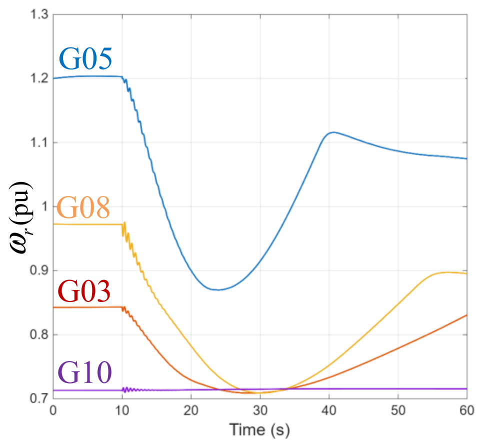

Figure 14. Wind turbine rotor speed vs. time under ΔP_d = 11.27 p.u.

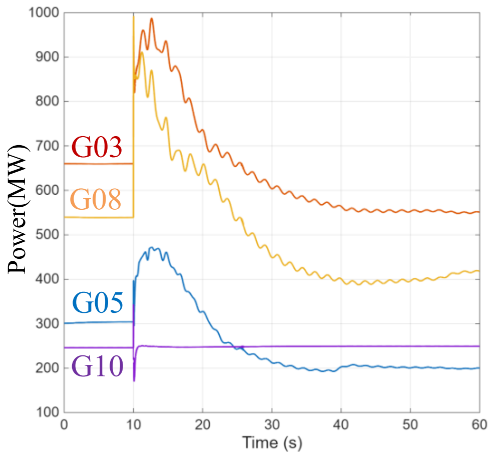

Figure 15. Wind turbine active power output vs. time under ΔP_d = 11.27 p.u.

Under the condition of frequency response solely from the wind farms, the maximum power disturbance ΔP_{dmax1} that the system frequency stability can withstand is 11.27 p.u. When ΔP_d = 6.44 is less than ΔP_{dmax1}, the primary FR meets the stability requirements. When ΔP_d is equal to ΔP_{dmax1}, based on the full utilization of the rotor kinetic energy of the wind farms, the occurrence of SFD is avoided, and the primary FR of the system is at the stability margin boundary. When ΔP_d = 12.236 is greater than ΔP_{dmax1}, the excessive response of the wind turbines triggers the speed recovery strategy, causing a severe SFD phenomenon in the system, with the frequency dropping to 48.47 Hz. The primary FR becomes severely unstable, posing a significant impact on the frequency stability of the power system.

When the fault disturbance ΔP_d exceeds ΔP_{dmax1}, the system frequency faces the risk of SFD, and the primary FR becomes unstable. Except for G05 (limited by the inverter's own power constraint), the rotational kinetic energy of the other wind farms is fully utilized and cannot provide additional active power support. Based on this simulation system, the EAL at Bus 04, Bus 15, and Bus 28 will participate in FR. The participation of EAL in the frequency response will alter the primary FR process. Assuming the EAL adopts virtual inertia-droop response control, the FR parameters are set as k_{H} = 4.0, k_{D} = 1.54. Under different step disturbances, the simulation results for the system are shown in Figure 16.

From Figure 16 above, it can be observed that the participation of EAL in FR significantly enhances the system's ability to withstand load disturbances. The equivalent UTFS parameters of the system are S_2(49.98,12.74,6.94,1.93). When ΔP_d = 11.27 p.u., the frequency nadir of the system rises from 49.3 Hz to 49.39 Hz. Simultaneously, the maximum load step that does not trigger relay protection action increases to 14 p.u. When both wind turbines and EALs jointly participate in frequency regulation, the system frequency stability region boundary increases from ΔP_d = 11.27 p.u. (when only wind turbines participate) to ΔP_d = 14 p.u. When the system withstands a load disturbance of 14 p.u. The active power output of the EAL and the rotor speed of the wind turbine are shown in Figures 17 and 18.

From the three vectors of the UTFS—S_0(10.13,8.32,16.94,9.98), S_1(45.56,12.92,4.71,9.93), and S_2(49.98,12.74,6.94,1.93)—the frequency stability regions of the system under different parameters can be calculated, as shown in Figure 19. The figure displays three frequency stability region boundaries. They correspond to the scenarios where wind turbines do not participate in FR, where wind turbines participate but EAL does not, and where both wind power and EAL jointly participate in FR. In the figure, ΔP_1, ΔP_2, and ΔP_3 represent the frequency stability region boundaries under three scenarios: neither wind turbines nor electrolytic aluminum loads participate in frequency regulation, only wind turbines participate, and both wind turbines and electrolytic aluminum loads participate in a coordinated manner, respectively. A comparison with time-domain simulations reveals that these boundaries closely match the maximum load steps observed in the simulations, demonstrating the correctness and practicality of the UTFS. Through the frequency stability region, the rate of change in frequency under boundary conditions can be determined. This allows the system to estimate the magnitude of a load disturbance early in the frequency decline phase and make rapid decisions proactively, enabling more stable, efficient, and economical FR by the EAL.

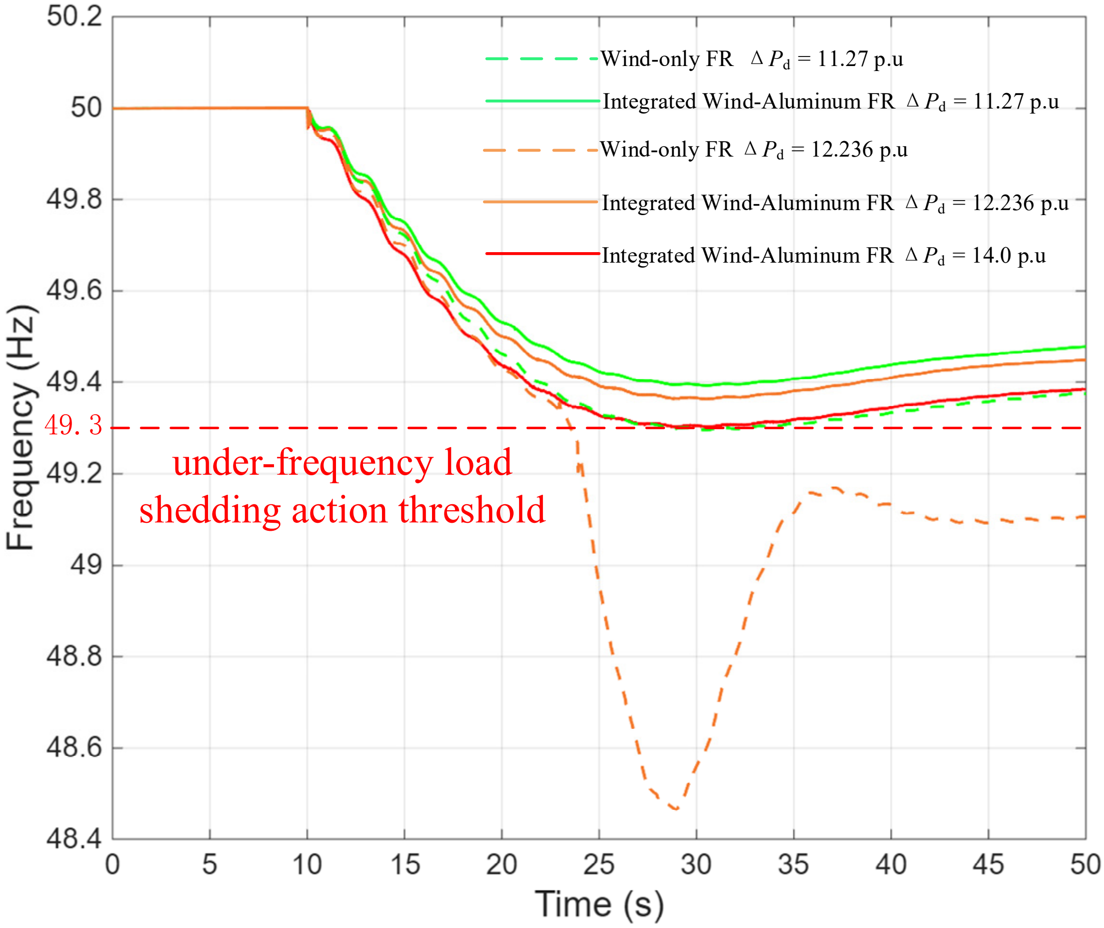

Figure 16. Frequency response curves under different load steps.

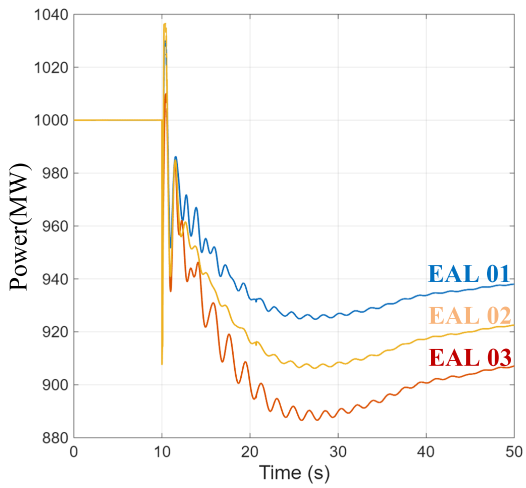

Figure 17. EAL active power output vs. time under $\Delta P_d = 14$ p.u.

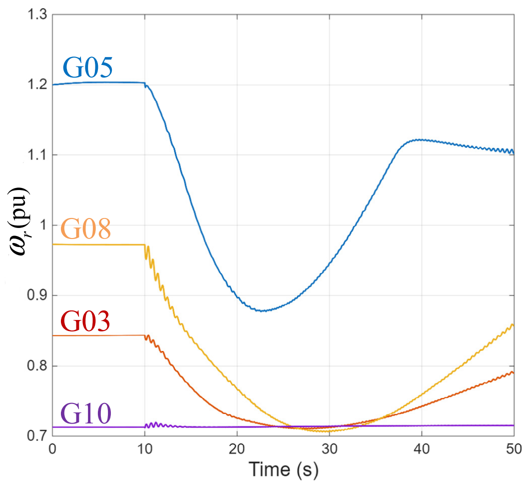

Figure 18. Wind turbine rotor speed vs. time under ΔP_d = 14 p.u.

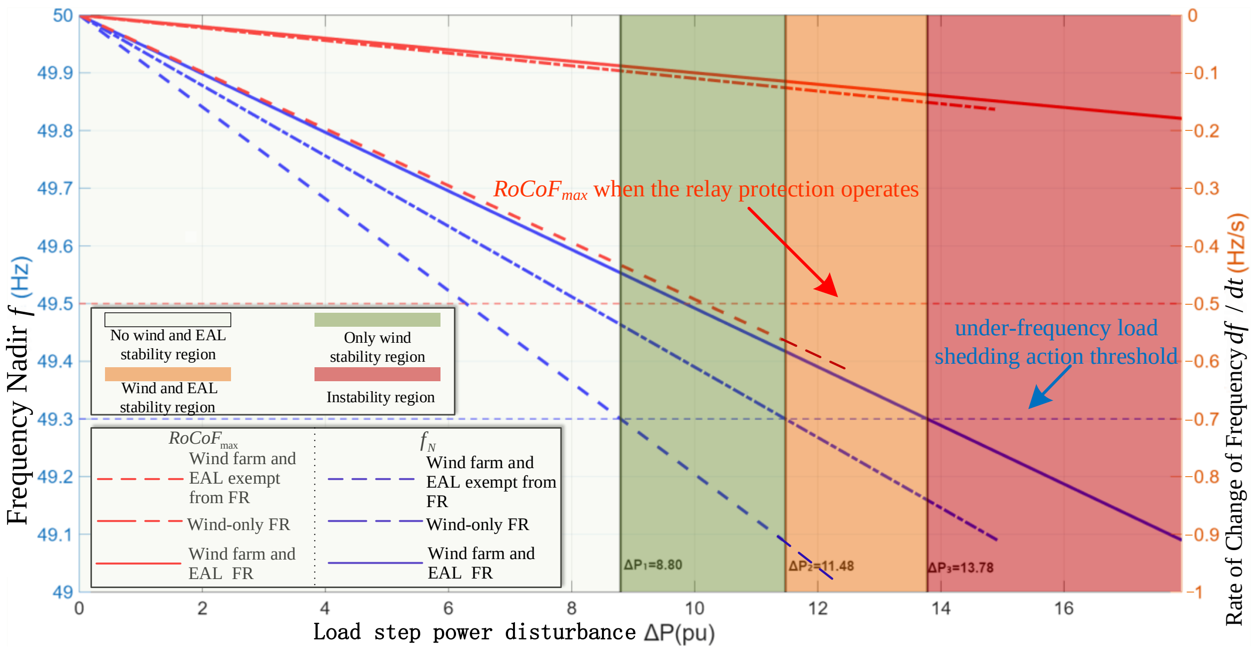

Figure 19. Frequency stability region diagram with different frequency regulation resources participating in system FR.

During wind turbine participation in system FR, the decision to activate EAL support is governed by real-time frequency dynamics. Specifically, when a rapid frequency decline is detected and the instantaneous absolute $RoCoF_{\max}$ exceeds the threshold $RoCoF_{\max}$ associated with $\Delta P_d = \Delta P_{d2}$ in Figure 19, EAL is triggered to contribute to FR. Conversely, if this condition is not satisfied, EAL remains inactive in order to preserve the economic efficiency of the industrial load.

6. Conclusions and Research Prospects

6.1. Conclusions

This paper proposes a coordinated FR control strategy integrating EAL and wind power while accounting for the SFD phenomenon. By developing a frequency response control scheme based on the load characteristics of EAL to regulate its active power, the following conclusions can be obtained:

- As an energy-intensive industrial load, EAL demonstrates considerable potential for FR. Through the adjustment of the saturable reactor, it can participate in primary FR while maintaining operational safety and avoiding significant disruption to normal production processes.
- The UTFS provides an effective framework for analyzing the frequency response of power systems in which both wind power and EAL participate in primary FR. It exhibits high accuracy in capturing the system frequency response trajectory as well as the active power–frequency characteristics of individual units.
- A coordinated FR framework integrating wind power and EAL is developed, in which the participation of EAL is determined by comparing the disturbance load magnitude with the predefined frequency stability region. This mechanism enables a balanced consideration of economic efficiency and power system security and stability.
- In a power system integrating wind power and EAL, the adaptive engagement of EAL in FR through controlled load reduction compensates for the limited regulation capacity of wind power operating independently. This coordinated approach effectively suppresses the SFD phenomenon induced by wind turbine rotor speed recovery.

6.2. Research Prospects

This study employs two primary frequency indicators to characterize the frequency stability region. By adopting UTFS as the analytical framework, the research methodology is streamlined and the boundary conditions governing EAL participation in system FR are quantitatively determined. The future research directions are outlined as follows:

- The EAL investigated in this study represents only one category of industrial load. Other types of industrial and non-industrial loads with potential frequency response capability have not been incorporated into the present analysis.
- The control strategies for wind turbines and EAL developed in this study are based on virtual inertia and virtual droop control schemes. In practical power systems, however, the coordinated operation of numerous additional components with more complex control mechanisms warrants further comprehensive investigation.
- The UTFS model cannot capture spatial frequency variations, disturbance propagation delays, or regional inertia heterogeneity. Future work will focus on extending UTFS to multi-area formulations and integrating network topology and wide-area measurements to better represent spatial dynamics in low-inertia power systems.

Author Contributions: Conceptualization, methodology, software, validation, formal analysis, investigation, resources, data curation, writing—original draft preparation, W.C.; writing—review and editing, F.T.; visualization, F.D.; supervision, project administration, Y.Y., B.L. and X.J. All authors have read and agreed to the published version of the manuscript.

Funding: This work was supported by the National Key Research and Development Program of China (No. 2023YFB2407300).

Institutional Review Board Statement: Not applicable.

Informed Consent Statement: Not applicable.

Data Availability Statement: The original contributions presented in this study are included in the article. Further inquiries can be directed to the corresponding authors.

Conflicts of Interest: Author Wei Chen was employed by the Yunnan Power Grid Co., Ltd. and Guangzhou Electric Power Trading Center Co., Ltd. The remaining authors declare that the research was conducted in the absence of any commercial or financial relationships that could be construed as a potential conflict of interest.

Abbreviations

The following abbreviations are used in this manuscript:

FR	Frequency regulation
SFD	Secondary frequency dip
EAL	Electrolytic aluminum load
UTFS	Unified transfer function structure
DFIG	Doubly fed induction generator
UFLS	Under frequency load shedding

References

1. National Development and Reform Commission; National Energy Administration; National Data Administration. *Action Plan for Accelerating the Construction of a New Type Power System (2024–2027)*; National Development and Reform Commission: Beijing, China; National Energy Administration: Beijing, China; National Data Administration: Beijing, China, 2024.
2. Meng, L.; Zafar, J.; Khadem, S.K.; Collinson, A.; Murchie, K.C.; Coffele, F.; Burt, G.M. Fast Frequency Response From Energy Storage Systems—A Review of Grid Standards, Projects and Technical Issues. *IEEE Trans. Smart Grid* **2020**, *11*, 1566–1581. [CrossRef]
3. Fernández-Guillamón, A.; Gómez-Lázaro, E.; Muljadi, E.; Molina-García, Á. Power systems with high renewable energy sources: A review of inertia and frequency control strategies over time. *Renew. Sustain. Energy Rev.* **2019**, *115*, 109369. [CrossRef]
4. de Almeida, R.G.; Castronouvo, E.D.; Peas Lopes, J.A. Optimum Generation Control in Wind Parks When Carrying Out System Operator Requests. *IEEE Trans. Power Syst.* **2006**, *21*, 718–725. [CrossRef]
5. Erlich, I.; Wilch, M. Primary Frequency Control by Wind Turbines. In *Proceedings of the IEEE Power and Energy Society General Meeting, Minneapolis, MN, USA, 25–29 July 2010*; IEEE: New York, NY, USA, 2010; pp. 1–8.
6. Tang, F.; Qi, J.; Liu, Z.; Guo, Y.; Deng, H. Quantitative Frequency Security Assessment of Modern Power System Considering All the Three Indicators in Primary Frequency Response. *Sustainability* **2023**, *15*, 13569. [CrossRef]
7. Hosseini, S.A.; Fotuhi-Firuzabad, M.; Dehghanian, P.; Lehtonen, M. Coordinating demand response and wind turbine controls for alleviating the first and second frequency dips in wind-integrated power grids. *IEEE Trans. Ind. Inform.* **2024**, *20*, 2223–2233. [CrossRef]
8. Qiao, Y.; Guo, X.; Lu, Z.; Sun, R. Parameter Setting Approach for Auxiliary Frequency Regulation of Wind Turbines Considering System SFD. *Power Syst. Technol.* **2020**, *44*, 807–815.
9. Fini, M.H.; Golshan, M.E.H. Determining optimal virtual inertia and frequency control parameters to preserve the frequency stability in islanded microgrids with high penetration of renewables. *Electr. Power Syst. Res.* **2018**, *154*, 13–22. [CrossRef]
10. Tang, X.; Cai, J.; Ma, S.; Xie, Y.; Chen, X. Impact of DFIG-based Wind Power Integration on Power System Frequency Response. *Proc. CSU-EPSA* **2020**, *32*, 37–43.
11. Tang, Y.; Yang, P.; Yang, Y. Frequency Response Control Strategy for Wind Turbines Considering SFD. *Autom. Electr. Power Syst.* **2023**, *47*, 166–174.
12. Tao, Y.; Yang, F.; He, P.; Li, C.; Ji, Y. Flexible Frequency Response Strategy for Wind Turbines Considering SFD and Speed Recovery. *Autom. Electr. Power Syst.* **2024**, *48*, 60–68.
13. Li, L.; Li, C. Yunnan's First Local Standard for Large User Grid-Connected Operation Officially Released. China Southern Power Grid News. Available online: https://www.csg.cn/epaper/epaper/nfdwb/html/2025-06/13/content_1796.htm (accessed on 13 June 2025).
14. Gao, P. Research on System Frequency Control Considering Combined Wind Power and Aluminum Load Participation. Master's Thesis, Kunming University of Science and Technology, Kunming, China, 2023.
15. Liao, S.; Zhang, M.; Xu, J.; Li, J.; Wang, X.; Ke, D.; Sun, Y.; Yu, J. A Frequency Stability Control Method for Power Grids Considering Static Voltage Stability Constraints with Participation of Aluminum Electrolysis Loads. *Proc. CSEE* **2022**, *42*, 6727–6740.
16. Nie, S.; Huang, R.; Chen, L.; Min, Y.; You, G.; Wu, C. Adaptive Primary Frequency Control of Electrolytic Aluminum Loads Considering Energy Recovery. *Autom. Electr. Power Syst.* **2024**, *48*, 37–45.
17. Anderson, P.M.; Mirheydar, M. A low-order system frequency response model. *IEEE Trans. Power Syst.* **1990**, *5*, 720–729. [CrossRef]
18. Gao, H.; Xin, H.; Huang, L.; Xu, T.; Ju, P.; Qin, X.; Huang, W. Common-Mode Frequency Analysis and Its Characteristic Quantification in Renewable Energy Power Systems. *Proc. CSEE* **2021**, *41*, 890–900.
19. Zhang, W.; Wu, C.; Huang, W.; Gao, H.; Chen, M.; Xin, H. System Frequency Characteristic Evaluation and Wind Power Frequency Regulation Parameter Tuning Considering S.F.D. *Autom. Electr. Power Syst.* **2022**, *46*, 11–19.

20. Nie, S.; Chen, L.; Min, Y.; Zhang, J.; Yin, F.; Wu, J.; Cui, D. Analysis of Primary Frequency Regulation Potential and Characteristics of Industrial Loads. *Power Syst. Technol.* **2023**, *47*, 3994–4005.
21. Bao, Y. Research on Frequency Regulation and Ancillary Service Strategy of High-energy-consumption Electrolytic Aluminum Loads Participating in Power System. Ph.D. Thesis, Wuhan University, Wuhan, China, 2019.
22. Zhang, Z. Research on Load Frequency Control Strategy for Interconnected Regional Power Grid Considering Participation of Electrolytic Aluminum Loads. Master's Thesis, Kunming University of Science and Technology, Kunming, China, 2022.
23. Bao, P.; Zhang, W.; Cheng, D.Y.; Liu, M. Hierarchical control of aluminum smelter loads for primary frequency support considering control cost. *Int. J. Electr. Power Energy Syst.* **2020**, *122*, 106202. [CrossRef]
24. Bao, Y.; Xu, J.; Liao, S.Y.; Sun, Y.; Li, X.; Jiang, Y.; Ke, D.; Yang, J.; Peng, X. Field verification of frequency control by energy-intensive loads for isolated power systems with high penetration of wind power. *IEEE Trans. Power Syst.* **2018**, *33*, 6098–6108. [CrossRef]
25. Sun, F. Fast Frequency Regulation of Power Systems with Controllable Loads. Master's Thesis, North China Electric Power University, Beijing, China, 2023.
26. Bao, P. Research on Source-Grid-Load Coordinated Active Power/Frequency Control Considering Response of Electrolytic Aluminum Loads. Master's Thesis, Shandong University, Shandong, China, 2021.
27. Rana, A.S.; Thomas, M.S.; Senroy, N. Wide Area Measurement System Performance Based on Latency and Link Utilization. In Proceedings of the 12th IEEE International Conference on Electronics, Energy, Environment, Communication, Computer, Control (E3-C), INDICON 2015, New Delhi, India, 17–20 December 2015. [CrossRef]
28. Xu, J.; Liao, S.; Sun, Y.; Ma, X.-Y.; Gao, W.; Li, X.; Gu, J.; Dong, J.; Zhou, M. An Isolated Industrial Power System Driven by Wind-Coal Power for Aluminum Productions: A Case Study of Frequency Control. *IEEE Trans. Power Syst.* **2015**, *30*, 471–483. [CrossRef]
29. Gao, H.; Xin, H.; Huang, L.; Li, Z.; Huang, W.; Wu, C.; Ju, P. Common mode frequency in converter-integrated power systems: Definition, analysis, and quantitative evaluation. *IEEE Trans. Power Syst.* **2022**, *37*, 4846–4860. [CrossRef]